Microsecond Timescale Simulations Suggests 5-HT mediated Pre-activation of the 5-HT_{3A} Serotonin Receptor

Nicholas B. Guros,[1,2] Arvind Balijepalli[2], and Jeffery B. Klauda[1,*]

[1]Department of Chemical and Biomolecular Engineering, University of Maryland, College Park, MD 20742, USA; [2]Biophyiscs Group, Microsystems and Nanotechnology Division, National Institute of Standards and Technology, Gaithersburg, MD 20899, USA;
[*]Corresponding author email: jbklauda@umd.edu

Classification: Biophysics and Computational Biology

Abstract

Aided by efforts to improve their speed and efficiency, molecular dynamics (MD) simulations provide an increasingly powerful tool to study the structure-function relationship of pentameric ligand-gated ion channels (pLGICs). However, accurate reporting of the channel state and observation of allosteric regulation by agonist binding with MD remains difficult due to the timescales necessary to equilibrate pLGICs from their artificial and crystalized conformation to a more native, membrane-bound conformation *in silico*. Here, we perform multiple all-atom MD simulations of the homomeric 5-hydroxytryptamine 3A (5-HT_{3A}) serotonin receptor for 15 – 20 μs to demonstrate that such timescales are critical to observe the equilibration of a pLGIC from its crystalized conformation to a membrane-bound conformation. These timescales, which are an order of magnitude longer than any previous simulation of 5-HT_{3A}, allow us to observe the dynamic binding and unbinding of 5-hydroxytryptamine (5-HT, i.e. serotonin) to the binding pocket located on the extracellular domain (ECD) and allosteric regulation of the transmembrane domain (TMD) from synergistic 5-HT binding. While these timescales are not long enough to observe complete activation of 5-HT_{3A}, the allosteric regulation of ion gating elements by 5-HT binding is indicative of a pre-active state, which provides insight into molecular mechanisms that regulate channel activation from a resting state. This mechanistic insight, enabled by microsecond-timescale MD simulations, will allow a careful examination of the regulation of pLGICs at a molecular level, expanding our understanding of their function and elucidating key structural motifs that can be targeted for therapeutic regulation.

Keywords: Molecular Dynamics, Ligand-gated Ion Channel, Priming or Pre-activation

1 Significance Statement

The pentameric ligand-gated ion channel 5-HT_{3A} exhibits a transient pre-active state that provides valuable insight into the binding and activation mechanisms of the ion channel. In this pre-active state, the allosteric regulation of the channel structure, and thereby function, upon ligand binding occur at timescales that are too fast to be measured experimentally. This study demonstrates the power of microsecond-timescale MD simulations in detecting these transitional pre-active states upon ligand binding and describing their effects on channel function at the molecular scale. Such a mechanistic understanding of the channel function is a critical element in the design of therapeutics for the regulation of 5-HT_{3A}, which are needed to reverse the effects of numerous pathological conditions.

2 Introduction

The homomeric 5-hydroxytryptamine 3A (5-HT_{3A}) serotonin receptor is a pentameric ligand-gated ion channel (pLGIC) located at the post-synaptic cleft that converts chemical signals to electrical responses in the central and peripheral nervous system (1, 2). The primary chemical signal responsible for 5-HT_{3A} activation is the neurotransmitter 5-HT (i.e. serotonin). The binding of 5-HT causes conformational changes in the structure of 5-HT_{3A} that permit the flow of ions through the channel formed between its five monomer subunits, generating an action potential at the post-synaptic cleft (3). Clinically, pLGICs including 5-HT_{3A} regulate physiological functions such as nausea and are implicated in numerous psychiatric disorders including major depressive disorder, post-traumatic stress disorder, and Parkinson's disease (4, 5). However, the mechanism by which agonist binding activates pLGICs and the structural basis that governs the transition between functional states is not well understood, and remains a critical element hindering the design of therapeutics for many psychiatric disorders (6, 7). This mechanism is postulated to be more complex than a simple binary binding by activating ligands to a pLGIC, instead requiring the 'priming' of a pLGIC by dynamic binding through transitional pre-active states (8, 9), a mechanism which is further supported by the conclusions of this work.

Molecular dynamics (MD) simulations are a useful technique for examining the basis of pLGIC function, including the mechanisms that govern rapid and dynamic transitions between states that cannot be observed through experimental techniques (10-12). Numerous pLGICs have been investigated using all-atom MD simulations, including the nicotinic acetylcholine (nAChR)

(13), glutamate-gated chloride channel (GluCl) (14), and glycine (GlyR) (15) receptors, which has provided valuable insight into the structural response of pLGICs to agonist binding. MD simulations of 5-HT_{3A} have only been performed more recently, since its structure (excluding the intrinsically disordered intracellular domain) was first reported using X-ray crystallography in 2014 (PDB ID: 4PIR (16)) and later through cryo-electron microscopy (cryo-EM) in 2018 (PDB ID: 6BE1 (17)). These *apo* structures, i.e. structures without 5-HT bound, have been reported as non-conductive (17-19), while more recently additional structures of 5-HT_{3A} have been resolved with various agonists and antagonists and have been reported as both conductive and non-conductive (18, 20). Such states are initially assigned based on pore radius through the channel, where a minimum pore radius greater than that of a given wetted ion, such as Na^+ or K^+, represents a pLGIC in a conductive state because it is sufficiently wide to permit the translocation of ions.

However, assigning states to these static structures is not trivial due to limitations in structural resolution, symmetry assumptions, removal of highly flexible residues, and the addition of molecular components that may artificially constrain the protein in a given conformation, such as the nanobodies used in the original crystallization of 5-HT_{3A} (16). Therefore, MD simulations are performed to confirm the assignment of a state using careful analysis of structural dynamics including the pore radius profile, changes to the agonist-binding regions, and changes to secondary structure elements in the TMD and extracellular domain (ECD). However, most simulations generally suffer from inadequately short timescales, usage of non-native membrane lipids, and a lack of validation of critical simulation parameters including protein equilibration, membrane equilibration, and ligand representation in a force field that if not properly validated, may bias a pLGIC in a non-native conformation, subsequently yielding an inaccurate assignment of channel state.

In this work, we performed all-atom MD simulations of both *apo* and 5-HT-bound 5-HT_{3A} starting with PDB ID: 4PIR (16) to determine the native protein state under conditions comparable with experiment (Figure 1A). The study builds upon previous MD simulations of full-length 5-HT_{3A} (18-20) in several notable ways. Firstly, each simulation was performed for $15 - 20$ μs, which is an order of magnitude longer than any previous simulations of 5-HT_{3A}. We demonstrate such timescales are necessary to adequately equilibrate 5-HT_{3A} using the CHARMM36 (C36) FF for lipids (21, 22) and for proteins (23) in a lipid membrane and to observe the dynamic nature of 5-HT binding during channel priming, i.e. observation of a pre-active state. Secondly, a ternary

lipid membrane composed of 1-palmitoyl-2-oleoyl-SN-glycero-3-phosphocholine (POPC), polyunsaturated 1-stearoyl-2-docosahexaenoyl-sn-glyerco-3-phosphocholine (SDPC), and cholesterol was used to mimic the neuronal lipid environment in which 5-HT_{3A} resides (24), whereas past simulations used only POPC to represent the lipid environment (18-20). The importance of lipid membrane type cannot be understated. It has been shown experimentally that cholesterol and polyunsaturated lipids interact directly with pLGICs such as nAChR (25-29), which is largely homologous in structure to 5-HT_{3A}, to strongly regulate receptor structure and conductance. Lastly, we included several levels of simulation validation to ensure our model accurately represents experiment, including sufficient lipid membrane equilibration to ensure realistic lipid packing and careful parameterization of 5-HT for the CHARMM General Force Field (CGenFF) (30) using free energy perturbation (FEP) simulations to determine its solvation free energy, ensuring the accurate representation of 5-HT binding to 5-HT_{3A}. We specifically highlight these two parameters because insufficient lipid packing can result in a reduction of protein-lipid interactions around the TMD and because improper ligand parameterization can result in an unrealistic affinity of 5-HT to the binding pocket of 5-HT_{3A}. Together, these simulations provide a framework for how microsecond-timescale MD simulations must be used to examine the equilibration of pLGICs from a crystalized conformation and to examine allosteric regulation from ligand binding that can help reveal the nature and functional state of the ion channel.

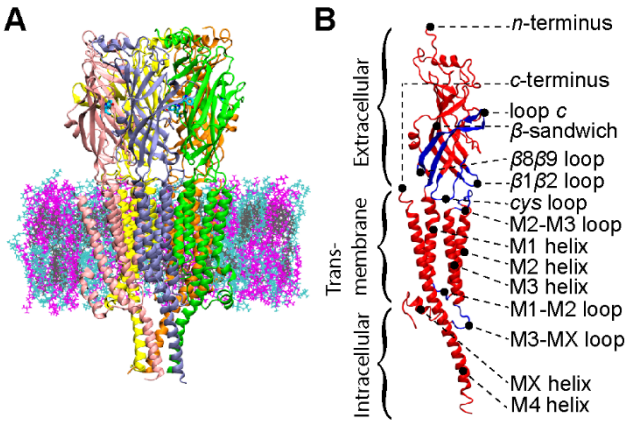

Figure 1. (A) Cross-section of 5-hydroxytryptamine 3A (5-HT_{3A}) in a lipid membrane with 5-HT_{3A} represented by secondary structure and colored by monomer *(A,* green; *B,* purple*; C,* pink*; D,* yellow*; E,* orange*)*, lipids represented as lines and lipid type represented by color: 1-palmitoyl-2-oleoyl-SN-glycero-3-phosphocholine (POPC), *cyan*; 1-stearoyl-2-docosahexaenoyl-sn-glyerco-

3-phosphocholine (SDPC), *magenta*; cholesterol, *gray*), and 5-HT also represented as lines (*aqua*). (B) A single monomer of 5-HT_{3A} represented by secondary structure and colored as red and blue to create contrast for specific secondary structure motifs.

3 Results

Accurately modeling the native structure of 5-HT_{3A} is an essential step to unraveling the structural elements that govern its function on a molecular level. To this end, we describe: the equilibration of 5-HT_{3A} from a crystalized conformation to a more native, membrane-bound conformation; the allosteric regulation of its TMD from dynamic binding of 5-HT to its principal binding pockets located on its ECD; and differences in systems with varied 5-HT concentration and lipid membrane composition. Table 1 defines the key parameters for these systems: three are composed of 5-HT_{3A} embedded in a POPC/SDPC/Cholesterol membrane without 5-HT (*apo*), with ≈ 5 mM 5-HT (five docked 5-HT), and with ≈ 15 mM 5-HT (five docked 5-HT plus ten 5-HT added to the aqueous phase). A fourth system is composed of 5-HT_{3A} embedded in a POPC membrane with ≈ 5 mM 5-HT (five docked 5-HT) to directly compare differences that arise from lipid membrane composition (Table 1). An example docking pose of 5-HT can be found in SI Appendix, Figure S1.

3.1 Equilibration and Stability

Both membrane and protein equilibration are critical for accurate simulations of membrane embedded transmembrane proteins. To demonstrate adequate membrane equilibration, the average surface area (SA)/lipid for the mixed (POPC/SDPC/cholesterol) and POPC membranes was calculated during 250 ns of system equilibration at constant pressure and temperature (NPT) until the moving average for each case converged to an equilibrium value (SI Appendix, Figure S2). For POPC, the equilibrium SA/lipid was (63.5 ± 0.5) $Å^2$, demonstrating good agreement with the experimental average of (62.7 ± 1.3) $Å^2$ (31), where the error bars represent the standard error. The average SA/lipid for the POPC/SDPC/cholesterol membrane was found to be (51.6 ± 0.4) $Å^2$, which is expectedly lower than the experimental SA/lipid of a pure POPC, due to the membrane condensing effects of cholesterol (32). Unless noted otherwise, all errors are defined as the standard deviation of the mean.

Adequate protein equilibration during microsecond production at constant volume and temperature (NVT) is demonstrated in Figure S3A through backbone root-mean-square deviation (RMSD) of 5-HT_{3A}, excluding the MX helix (located at the terminus of the M3 helix, see Figure 1). Figure S3A demonstrates that all three 5-HT-bound structures stabilize by 10 μs in both mixed and POPC membranes (as listed in Table 1), whereas 5-$HT_{3A\text{-}Apo}$ stabilizes by 14 μs. The additional equilibration time in the *apo* case is likely due to increased flexibility of loop *c* of the binding pocket that is stabilized through 5-HT binding in the other systems. The MX helix was excluded from the backbone RMSD because it is highly flexible due to the lack of 57 intracellular and intrinsically disordered residues linking it to the M4 helix that were unresolved during the crystallization of 5-HT_{3A} (16). RMSD per secondary structure element (where definitions by residue number can be found in Table S1) was also calculated and is shown in SI Appendix, Figure S4 to demonstrate the highly flexible nature of the MX helix compared to the other secondary structure elements.

Backbone RMSD for the ECD (Figure S3B) and TMD (Figure S3C) was also calculated to assess the structural response in the ECD to 5-HT binding and subsequent allosteric regulation of the TMD. Differences in the ECD RMSD trends for 5-$HT_{3A\text{-}Apo}$ and 5-$HT_{3A\text{-}15mM}$ are unremarkable (Figure S3B). ECD RMSD for 5-$HT_{3A\text{-}5mM\text{-}POPC}$, on the other hand, demonstrates a distinct departure from the other three trends between 2 – 3 μs (Figure S3B). However, this departure does not appear correlated to a departure in TMD RMSD (Figure S3C) and can be explained by rapid opening and closing of the flexible loop *c* on multiple monomers which ultimately does not result in allosteric regulation of the TMD. Conversely, ECD RMSD for 5-$HT_{3A\text{-}5mM}$ demonstrates a distinct departure from the other three trends between 5 – 10 μs (Figure S3B) which appears correlated to a distinct departure in TMD's RMSD between 5 – 10 μs (Figure S3C). RMSD per secondary structure element is shown in SI Appendix, Figure S5, including the elements that contribute most significantly to this departure, including the M2-M3 loop, the *cys*-loop, and the β8-β9 loop, which exist at the interface between the ECD and TMD and are reported to be involved in the allosteric activation of 5-HT_{3A} (6, 18, 33). We subsequently explored the cause of these departures in 5-$HT_{3A\text{-}5mM}$ RMSD, specifically as to how they relate to allostery between the binding of 5-HT to its principal binding pockets on the ECD and resultant structural shifts between domains, as discussed further in section 3.4.

3.2 Structural Overview

The assignment of ion channel state between conductive and non-conductive is generally determined through the pore radius profile which demonstrates the pathway available for ion translocation through the channel (see *Analysis Methods* in *Supporting Material*). In Figure 2A, pore radius profiles are shown for the initial crystal structure, PDB ID: 4PIR (16), (*light blue, dashed*) and for 5-$HT_{3A\text{-}Apo}$ (*orange*) averaged over 20 μs after the 250 ns of equilibration from the crystal structure, where the standard error of the pore radius is within the thickness of the trend line. PDB ID: 4PIR is non-conductive because while the entire ECD is hydrated and accessible to ion translocation, the minimum pore radius is < 2 Å through the TMD (*gray*), below the threshold needed to permit the passage of hydrated K^+ ions. SI Appendix, Figure S6 clearly shows the contrast between PDB ID: 4PIR and an open conformation of 5-HT_{3A} (PDB ID: 6HIN (20)), which would permit the translocation of ions with a slight movement of pore-lining helices and the L260 sidechain.

The minimum pore radius along the ECD of 5-$HT_{3A\text{-}Apo}$ deviates by less than 1 Å from the crystal structure. This allows the ECD to remain hydrated and thereby accessible to ion translocation. However, the pore closes across the TMD (−50 Å < z < 0 Å) as demonstrated by the pore radius approaching a minimum value of 0 Å for 20 μs of simulation time (Figure 2A, *gray* region). Furthermore, the snapshot of the TMD shown in Figure 2B reveals that symmetry is maintained between the M2 helices of each monomer in this closed conformation, as depicted by the red-dashed line connecting the centers of the pore-lining M2 helices and shown in the associated plot of the interior angle θ for each of the five monomers (Figure 2C). Any fluctuations in the orientation appear cooperative and mostly in parallel to these lines of symmetry, as opposed to orthogonal to the center of the pore. Figure 2D shows the lifecycle of activation for 5-HT_{3A} and indicates that this conformation is most consistent with a non-conductive resting state; however, a post-desensitized state cannot be ruled out, which is also functionally non-conductive, but exists after the activation and desensitization of 5-HT_{3A} and is unresponsive to 5-HT binding.

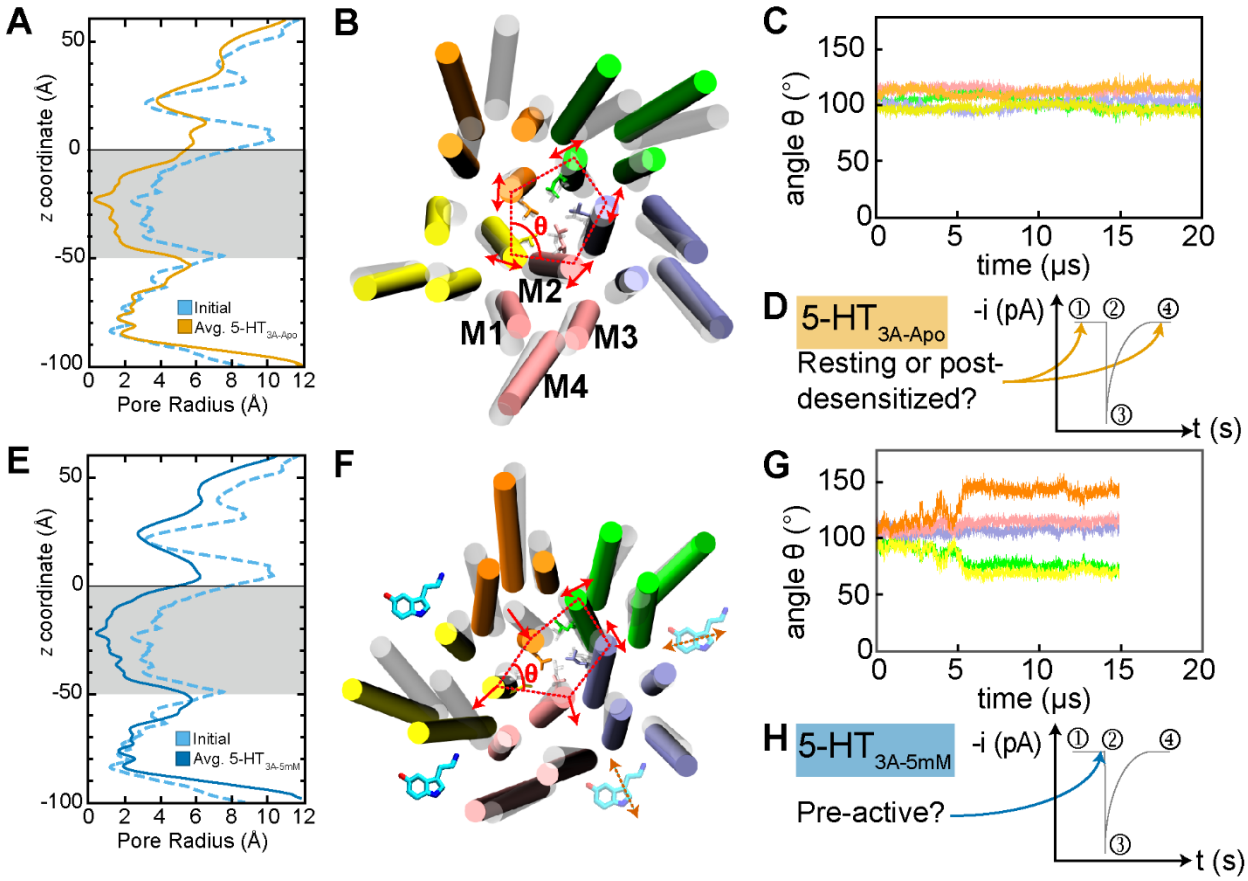

Figure 2. (A) Pore radius profiles for the starting structure (*light blue, dashed*) and 5-HT$_{3A\text{-}Apo}$ (*orange*) averaged over 20 μs with the transmembrane domain (TMD) shaded *gray* and error bars smaller than the thickness of the profile trend. (B) TMD snapshot for 5-HT$_{3A\text{-}Apo}$ (including L260) shown as secondary structure and lines (respectively), with the initial structure as transparent white and the final structure colored by monomer (A, *green;* B, *purple*; C, *pink*; D, *yellow*; E, *orange*), with lipids, water, and ions removed for clarity. Representative helix labels for M1-M4 shown for monomer C with red, dashed lines connecting the centers of pore-lining M2 helix to demonstrate symmetry and *red*, solid arrows indicating the principal direction of M2 fluctuation. (C) Interior angle θ for the five monomers in (A) versus time. (D) Representative trend of current (*i,* pA) versus time (*t,* s) for the lifecycle of a 5-HT$_{3A}$ receptor with instantaneous currents shown for the resting (1), pre-active (2), activated/open (3), and desensitized (4) states. Arrows indicate the possible states suggested by 5-HT$_{3A\text{-}Apo}$. (E) Pore radius profiles for the starting structure and 5-HT$_{3A\text{-}5mM}$ (*blue*) averaged over 15 μs with the TMD shaded in *gray* and error bars smaller than the thickness of the profile trend. (F) TMD snapshot of 5-HT$_{3A\text{-}5mM}$ depicted the same as (C) with cartoon 5-HT indicating 5-HT-binding between monomers for the entire 15 μs (*solid*) and transient binding (*transparent with dashed arrows*). (G) Same as for (C), but for 5-HT$_{3A\text{-}5mM}$. (H) Same as for (D), but for 5-HT$_{3A\text{-}5mM}$.

In Figure 2E, pore radius profiles are shown for the initial crystal structure, PDB ID: 4PIR, (*light blue, dashed*) and for 5-HT$_{3A\text{-}5mM}$ (*blue*) averaged over 15 μs after the 250 ns of equilibration from the crystal structure, where the standard error of the pore radius is within the thickness of the trend line. The average minimum pore radius along the ECD of 5-HT$_{3A\text{-}5mM}$ deviates by less than

1 Å from the crystal structure, but remains hydrated and accessible to ion translocation (Figure 2E). Similarly to $5TH_{3A\text{-}Apo}$, the pore radius across the TMD (-50 Å $< z <$ 0 Å) approaches a minimum value of 0 Å and the pore remains closed for 15 μs (Figure 2E, *gray* region). Alone, this result suggests that the presence of bound 5-HT only impacts the ECD and not the TMD of 5-HT_{3A}, suggesting a lack of allostery and a desensitized state of 5-HT_{3A}. However, in Figure 2F a snapshot of the TMD of 5-$HT_{3A\text{-}5mM}$ demonstrates that there is a significant antisymmetric shift between monomers D (*yellow*) and E (*orange*). Such an antisymmetric shift is depicted by a similar M2 helix center connecting red-dashed line and red arrows to demonstrate the direction of monomer shift conversely to the symmetric closure observed in 5-$HT_{3A\text{-}Apo}$ and by the associated plot of the interior angle θ for each of the five monomers (Figure 2G) that demonstrates significant deviations in interior angle symmetry. The shift begins around 5 μs and appears correlated to the departures in RMSD of both the ECD and TMD at around 5 μs (Figures S3B and S3C). The shift dynamics can be summarized as follows: M2-D shifts outwards from the center of the pore in a cooperative fashion with M1-D, M3-D, and M4-D (M2-C also displays an outward shift, but to a lesser extent), which would result in incremental pore opening if not for M2-E subsequently shifting inwards toward the center of the pore in a cooperative fashion with M1-E, M3-E, and M4-E and occupying the space voided by M2-D, resulting in the final conformation shown in Figure 2F. M2-A and M2-B display fluctuations parallel to the pore center similar to the M2 helices of 5-$HT_{3A\text{-}Apo}$.

Shown schematically in Figure 2F, 5-HT binds within binding pockets (bp) formed between pairs of monomers in the ECD (removed for clarity), for example bpCD is formed between the complementary monomer C and primary monomer D, while bpDE is formed between complementary monomer D and primary monomer E (an example of the initial binding pose in shown in SI Appendix, Figure S1). The asymmetric shifts observed in 5-$HT_{3A\text{-}5mM}$ appear correlated to 5-HT binding in these binding pockets. Monomer D is bound on either side by two 5-HT, and subsequently undergoes a conformational change as described in the previous paragraph. On the other hand, monomer C is only bound by 5-HT on its complimentary face and subsequently displays a minor M2 conformational change, while monomer E is only bound by 5-HT on its primary face and subsequently displays significant M2 collapse into the channel. Furthermore, Figure 2F shows that monomers A and B do not undergo observable conformational changes, and do not appear to be allosterically regulated by 5-HT. We find that 5-HT only rebinds transiently to bpAB and bpBC and does not rebind substantially to bpEA, in contrast to the binding

observed in bpCD and bpDE. Because the conformational changes caused by the binding of only two 5-HT does not result in the channel opening sufficiently to permit the translocation of ions (9, 34), we cannot assign an activated state to the simulated conformation 5-HT_{3A}. However, because this 5-HT binding causes conformational changes to a single monomer of 5-HT_{3A} that resemble the initialization of channel opening, we conclude that 5-HT appears to be priming the receptor for activation, i.e. the conformation resembles a pre-active state, as indicated by in Figure 2H, and not a desensitized or post-desensitized state.

Symmetric pore closure is also observed in 5-$HT_{3A\text{-}5mM\text{-}POPC}$ and in 5-$HT_{3A\text{-}15mM}$ (SI Appendix, Figure S7), similar to 5-$HT_{3A\text{-}Apo}$. In 5-$HT_{3A\text{-}5mM\text{-}POPC}$ (SI Appendix, Figure S7A), only one 5-HT is bound over the duration of the simulation and no large conformational change is observed in the TMD, suggesting that the binding of a single 5-HT is also insufficient to cause channel opening or even priming of the channel. However, monomer D of 5-$HT_{3A\text{-}15mM}$ (SI Appendix, Figure S7B, *yellow*) is bound on either side by 5-HT, similar to 5-$HT_{3A\text{-}5mM}$, but does not demonstrate a large outwards shift in M2-D from the center of the pore, in contrast to the shift observed for M2-D of 5-$HT_{3A\text{-}5mM}$. Subsequently, we explored the nature of the binding events at each 5-HT concentration to determine differences in 5-HT binding which result in different apparent outcomes with respect to monomer D between these two systems. Additionally, a full comparison of the TMD conformations for all four systems compared to the open conformation (PDB ID: 6HIN) is shown in SI Appendix, Figure S8.

3.3 5-HT Binding Events

Numerous binding events were observed in 5-$HT_{3A\text{-}5mM}$ and 5-$HT_{3A\text{-}15mM}$ throughout each 15 μs simulation. Here, we define binding as when 5-HT is within 4 Å of the ECD of 5-HT_{3A} for at least 50 ns to exclude inconsequential collisions between the two biomolecules. Binding events ranged from completely stable to transient, in some cases lasting the entire 15 μs simulation time. The number of 5-HT molecules bound to 5-HT_{3A} at a given point in time are plotted in Figure 3A for 5-$HT_{3A\text{-}5mM}$ and SI Appendix, Figure S9A for 5-$HT_{3A\text{-}15mM}$. While initial docking orientations and binding energies were nearly identical after the 250 ns equilibration (which resulted in minor structural changes to the binding pocket, see *Methods*), bound 5-HT ultimately sampled a range of conformations in each of the five binding pockets where the stability of each binding event varied substantially between orientations.

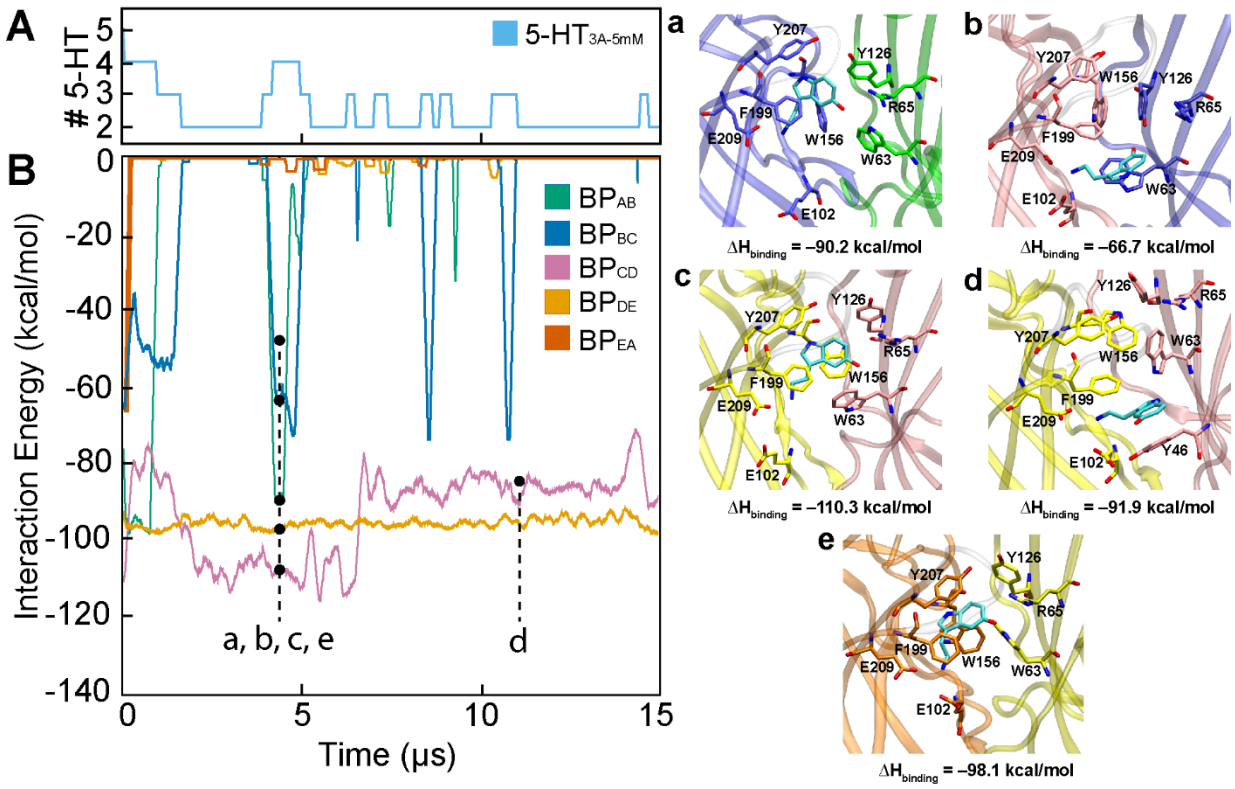

Figure 3. (A) Total binding events of 5-HT with 5-HT$_{3A\text{-}5mM}$. (B) enthalpic contribution to binding energy between 5-HT and the extracellular domain (ECD) where letters correspond to binding orientations on the right: bpAB (a, ≈ 4.6 μs), bpBC (b, ≈ 4.6 μs), bpCD (c, ≈ 4.6 μs), bpCD (d, ≈ 14.7 μs), and bpDE (e, ≈ 4.6 μs) and monomers colored as: A, *green;* B, *purple*; C, *pink*; D, *yellow*; E, *orange*.

For 5-HT$_{3A\text{-}5mM}$, bpCD and bpDE were occupied by a single 5-HT for the duration of the simulation, whereas bpAB and bpBC experienced transient binding of 5-HT, i.e. several instances of binding and rebinding for different durations (Figure 3B). bpEA experienced no significant binding events after the unbinding of 5-HT within the first 50 ns, due likely to the opening of loop *c* on monomer A which contributes substantially to the stability of 5-HT in the binding pocket and which remained in an open conformation for the duration of the simulation. Binding poses corresponding to the five markers in Figure 3B are shown for bpAB, bpBC, bpCD, and bpDE in Figure 3 with panel letters corresponding to the marker letter. Four binding poses are shown at around 4.6 μs, where the highest number of 5-HT are bound (four) for ≈ 1 μs, which occurs immediately prior to structural changes in the ECD and TMD demonstrated in Figures 2 and S3. Lastly, a binding pose at around 11.4 μs is shown for bpCD to demonstrate a significant change in binding orientation not observed for bpDE that is stable for the duration of the simulation and

suggests an alternative binding pocket for 5-HT which could be related to the binding dynamics of pre-activation.

Each panel in Figure 3 depicts the residues of 5-HT_{3A} involved in the binding of 5-HT, residues that are generally conserved between events with some exceptions. For bpAB (where transient binding is observed), E209 of the primary monomer forms a salt bridge with the amine group of 5-HT, the hydroxyl group of 5-HT only experiences transient stabilization through charge-dipole interactions with R65, and the indole group experiences only transient stabilization through effective π-π stacking with Y207 and F199 (Figure 3a). Meanwhile, bpBC displays dual electrostatic stabilization of 5-HT through E209 and E102, but only transient π-π stacking with W63 and F199 and has virtually no interaction with R65 (Figure 3b). The transient binding in these pockets appears to be governed by the breaking of a salt bridge between D202 of the primary monomer and R65 of the complimentary one; loop *c* of the primary monomer locks at the salt bridge, over the binding pocket (SI Appendix, Figure S10). Because binding-pocket residues Y207, W156, F199, and E209 are located on loop *c*, it is not surprising that only transient binding is observed when loop *c* opens from the binding pocket, whereas loop *c* remains locked by the D202-R65 salt bridge for bpCD and bpDE.

The binding poses for bpCD and bpDE are nearly identical at around 4.6 μs, with E209 and E102 interacting electrostatically with the amine group of 5-HT and R65 and the hydroxyl group of 5-HT interacting through charge-dipole interactions (Figure 3c and 3e). Simultaneously, the indole group of 5-HT is stabilized through π-π stacking with W156 and F199 and occasionally with Y207. The aforementioned D202-R65 salt bridge keeps loop *c* residues Y207, F199, and E209 near the binding pocket's complimentary residues and ultimately enables more residues to stabilize 5-HT in the pocket (SI Appendix, Figure S10). Lastly, Figure 3e shows that the binding orientation for bpCD results in a decrease in the enthalpic contribution starting at around 7.2 μs, but is still sufficiently stable to maintain a bound conformation with 5-HT_{3A}. A similar electrostatic stabilization between the amine group of 5-HT and E209 and E102 is observed, however the only other stabilization interactions are π-π stacking with Y46 and transient π-π stacking with F199.

Presumably, the additional 5-HT in 5-$HT_{3A\text{-}15mM}$ (SI Appendix, Figure S9A) would yield better activation than in 5-$HT_{3A\text{-}5mM}$; however, due to conflicts between multiple 5-HT in a single binding pocket and channel blocking (SI Appendix, Figure S11), better activation was not achieved. Experimentally, concentrations as low at 10 μM are used yield complete channel activation (9,

34), but achieving such a low concentration *in silico* would require an impractical volume of water for MD simulations. Notably, the enthalpic contributions to binding energy in 5-$HT_{3A\text{-}5mM}$ for bpCD and bpDE are more favorable than any of the sustained (and most of the transient) binding events observed in 5-$HT_{3A\text{-}15mM}$ (SI Appendix, Figure S9B). For example, 5-HT is bound to bpAB for over 10 μs in 5-$HT_{3A\text{-}15mM}$ (SI Appendix, Figure S9a), initially bound in an orientation as favorable as bpDE in 5-$HT_{3A\text{-}5mM}$. However, this orientation shifts to one where 5-HT is bound only to the bottom interface of the binding pocket (SI Appendix, Figure S9b), resulting in an interaction with only a single conserved binding residue (E209) and an enthalpic contribution to binding energy of ≈ −40 kcal/mol. Binding pockets bpCD and bpDE, which are also occupied for a large portions of the simulation, demonstrate similarly unfavorable orientations (SI Appendix, Figure S9e and S9g), which is a possible explanation that while sustained, these binding events do not result in the outward M2 shifts observed in 5-$HT_{3A\text{-}5mM}$ and why evidence of pre-activation was not readily observed in 5-$HT_{3A\text{-}15mM}$. Binding orientations with enthalpic contributions to binding energy on par with those for bpCD and bpDE of 5-$HT_{3A\text{-}5mM}$ are also observed in 5-$HT_{3A\text{-}15mM}$ (Figures S9c, S9d, S9f, and S9h), however these events are not as long in duration as those in 5-$HT_{3A\text{-}5mM}$, further explaining why M2 shifts indicative of pre-activation are not observed in 5-$HT_{3A\text{-}15mM}$. Moreover, the salt bridge between R65 and D202 was not maintained for any of the binding pockets in 5-$HT_{3A\text{-}15mM}$, resulting in the opening of loop *c* to various extents in all five binding pockets. Notably, 5-HT remained bound in several instances without the additional stability provided by loop *c*, but these events appeared insufficient with respect to allosterically converting 5-HT binding to changes in the TMD. Subsequently, we have presented specific residue-based evidence for the allosteric mechanism by which the binding events observed in bpCD and bpDE of 5-$HT_{3A\text{-}5mM}$ regulate structural shifts in the TMD of monomer D as they relate to pre-activation, and possible causes for the inwards collapse of M2-E.

3.4 Domain Interactions

The mechanism that governs the transition between states of 5-HT_{3A} lies in the allostery between 5-HT binding and secondary structure elements in the TMD and ECD, namely the M2-M3 loop (TMD), the β1-β2 loop (ECD), the β8-β9 loop (ECD), and the pre-M1 region (TMD/ECD) (6, 18, 33), which are shown for 5-$HT_{3A\text{-}5mM}$ monomers C, D, and E in Figure 4A. The β1-β2 loop, the β8-β9 loop, and the pre-M1 region are all directly connected to residues

involved in 5-HT binding through β-strands and all interact either directly or indirectly with the M2-M3 loop. The M2-M3 loop is critical to channel gating because it acts as a spring that regulates the orientation M2, which is critical because separation between neighboring M2 helices is needed to allow the turning of L260 away from the center of the pore (shown in an open conformation PDB ID: 6HIN (20) as an indication of a conductive state, SI Appendix, Figure S6), and outwards tilt and/or translation of M2 allows this separation of helices to occur. The M2-M3 loop has been reported as natively restrained in the *apo* form (18), which we also observe in this work, meaning that pore opening is an active process that requires the release of the loop from a native restraint.

The disparity between the conformational change observed in monomer D and the collapse observed in monomer E initiates with the M2-M3 loop which in monomer D coils into a helix that causes M2-D to tilt outwards along with M3-D (Figure 4A). The opposite occurs in the M2-M3 loop of monomer E which becomes more elongated allowing M2-E to tilt inwards along with M3-E. Coiling of M2-M3-D is permitted because of a shift in β1-β2-D away from M2-M3-D (and towards β1-β2-E), while β1-β2-E and β1-β2-C do not demonstrate significant shifts (Figure 4A). Distances between the center of masses of the five β1-β2 loops are shown in Figure 4B for $5\text{-HT}_{3A\text{-}5mM}$ to demonstrate the deviation from the average distance between β1-β2 loops and the distances between β1-β2-D and its neighbors and in Figure 4C for $5\text{-HT}_{3A\text{-}Apo}$ which serves as a control case (no 5-HT is bound). We propose that of the β1-β2 loops, only β1-β2-D shifts because bpDE residues D-Y46, D-W63, and D-R65 all lie on β-strands 1 and 2 of monomer D which at the onset of binding are pulled toward the primary monomer E through 5-HT in bpDE as the intermediary, while the pentameter D residues of bpCD are pulled toward the complimentary monomer *C* through 5-HT in bpCD as the intermediary, causing a twisting of monomer D which includes twisting of β1-β2-D. Neither monomers C or E are bound on either side by 5-HT, so they do not display the same twisting as seen in monomer D, but rather are constrained in only one direction by 5-HT binding. Moreover, this twist of monomer D and coiled orientation of M2-M3-D is stabilized by a salt bridge that forms between D271 of M2 and K54 of β1-β2-D which locks monomer M2-D in a conformation that reduces channel occlusion (Figure S12A). Alternatively, because β1-β2-E does not exhibit a twisting motion, K54 of monomer E is stabilized by forming a salt bridge with D52 and E53 of β1-β2-D when β1-β2-D twists toward β1-β2-E (Figure 4A). The twisting of β1-β2-D further allows D271 of M2-E to also form a salt bridge with K54 of monomer

D, but unlike D271 of M2-D, this salt bridge constrains M2-E in an orientation that creates channel occlusion instead of decreasing restriction through the channel (Figure S12B).

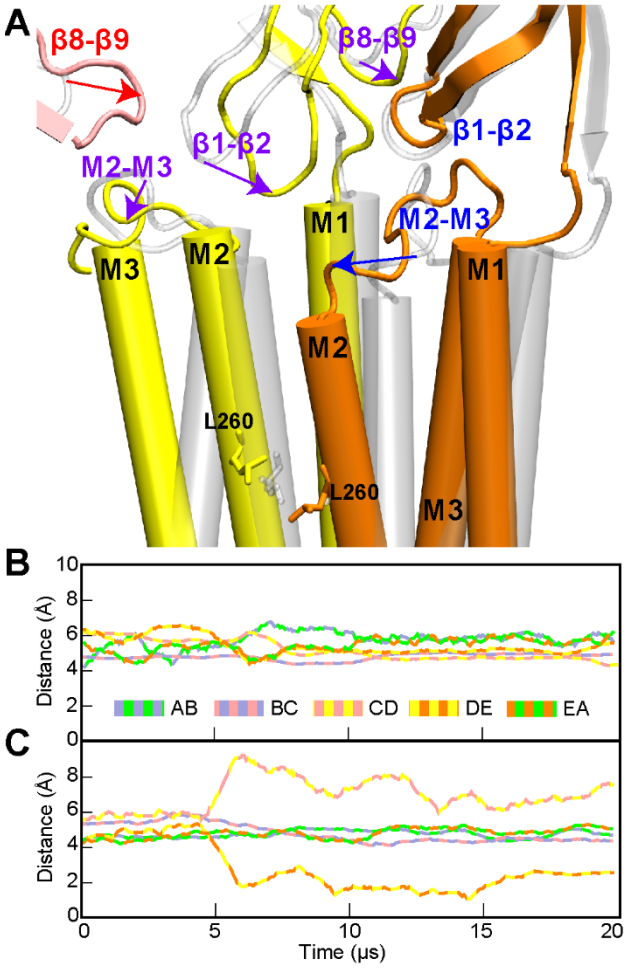

Figure 4. (A) Principal shifts in secondary structure motifs at the transmembrane domain (TMD)/extra cellular domain (ECD) interface for 5-HT$_{3A\text{-}5mM}$ due to sustained binding events in bpCD and bpDE. Monomers C (*pink*), D (*yellow*), and E (*orange*) shown as secondary structure with initial structures colored as transparent white. Monomers A and B, and all M4 helices removed for clarity. Distances between the center of masses of the β1-β2 loops colored by monomers for 5-HT$_{3A\text{-}Apo}$ (B) and 5-HT$_{3A\text{-}5mM}$ (C).

Additionally, differences in shifts observed in the β8-β9 loops of monomers C and D appear to play a role in stabilizing the conformation of monomer D that reduces channel occlusions and the conformation of monomer E that increases it. The M2-M3 loop is natively constrained by hydrogen bonding to the β8-β9 loop and pre-M1 region of the complimentary monomer,

constraints which are broken, but then reconfigured between T276 of M2-M3-D and Q184 of β8-β9-C in the form of hydrogen bonding (Figure S12C). However, due to an upwards shift in β8-β9-D as a result of twisting observed in monomer D, T276 of M2-M3-E and E186 of β8-β9-D also form a hydrogen bond (Figure S12D), but much like the D271-K54 salt bridge, this hydrogen bond contributes to lock M2-M3-D in an conformation that reduces channel occlusion and M2-M3-E in a conformation that increases it. In both cases a salt bridge is formed between E186 and R218 (Figure S12C-D) which strengthens the configurations governed by hydrogen bonding with T276.

In summary, bound only to the primary face of 5-$HT_{3A\text{-}5mM}$ monomer C, 5-HT appears to regulate the β8-β9 loop which is connected through β-strand linkage to the primary face, but not to the β1-β2 loop which is only connected to the complimentary face (Figures 4 and S12). Conversely, bound only to the complimentary face of 5-$HT_{3A\text{-}5mM}$ monomer E, 5-HT appears to regulate the β1-β9 loop which is connected through β-strand linkage to the complimentary face, but not to the β8-β9 loop which is only connected to the primary face, preventing the M2-M3-E loop from expanding outwards, and allowing M2-E to collapse inwards (Figures 4 and S12). Only in the case of 5-$HT_{3A\text{-}5mM}$ monomer D, do we report full allosteric regulation and activation of a 5-HT_{3A} monomer in contrast to its neighboring monomers which are only partially bound by 5-HT. Significant shifts of these loops in the other monomers of 5-$HT_{3A\text{-}5mM}$ and in the three other systems were not observed, indicating that the binding of 5-HT that allosterically regulates monomer D of this system is indicative of pre-activation, whereas at least three bound 5-HT are required to achieve complete activation (9, 34).

Lastly, changes in the TMD are not solely related to agonist binding in pLGICs, and can also be regulated by antagonists, glycosylation, phosphorylation, and the lipid membrane itself. This last effect of lipid interactions is relevant to the conformational transition of monomer D in 5-$HT_{3A\text{-}5mM}$. Therefore, we subsequently discuss the differences between the three systems with a membrane composed of a 7:7:6 mixture of POPC/SDPC/cholesterol and the final system with a membrane composed of pure POPC, as defined in Table 1.

3.5 Impact of Lipid Type

This work is unique compared to past simulations of 5-HT_{3A} because the simulations performed here are the first to use a lipid membrane composition representative of a neuronal membrane (a 7:7:6 mixture of POPC/SDPC/cholesterol) and the first to compare simulations of a

pLGIC in two different membrane lipid compositions (this mixture versus pure POPC). POPC is commonly used for simulations of mammalian proteins because it is considered representative of mammalian lipid membranes, however both polyunsaturated fatty acid (PUFA) lipids such as SDPC and cholesterol have been found to make up a significantly high percentage of the lipids found in 5-HT_{3A}-containing membranes (25). While to date there is a lack of evidence demonstrating the direct effects of these lipids on 5-HT_{3A}, there is evidence demonstrating that these lipids interact directly with and regulate the function of other pLGICs such as the nAChR, the *Gloeobacter violaceus* ligand-gated ion channel (GLIC), and the γ-aminobutyric acid receptor (GABA), which are largely homologous in structure to 5-HT_{3A} (25-29, 35-38). This indicates a need to study the effects of these lipids on 5-HT_{3A} to determine if they play a role in regulating its function similar to other pLGICs. Therefore, we report differences in lipid distribution and lipid interaction with 5-HT_{3A} between 5-$HT_{3A\text{-}5mM}$ and 5-$HT_{3A\text{-}5mM\text{-}POPC}$, as depicted by representative snapshots for the two simulations in Figure 5A and 5B, respectively. The first observable difference in lipid distribution is greater clustering of SDPC (*cyan*) compared to POPC (*magenta*) around the TMD of 5-$HT_{3A\text{-}5mM}$, quantified by the average number of SDPC within 3.5 Å of 5-HT_{3A} (46.2 ± 0.03) compared to POPC (35.6 ± 0.02). SDPC demonstrates a tendency to transiently penetrate the TMD with its saturated chain (Figure 5A, small *red* circle), in contrast to POPC (Figures 5A-B). The TMD of each 5-$HT_{3A\text{-}5mM}$ monomer is transiently penetrated by at least one SDPC (with the exception of monomer E), as shown in SI Appendix, Figure S13. Sustained penetration of the TMD is only observed in the 5-$HT_{3A\text{-}5mM}$ monomer D (Figure 5A, large *red* circle), which experiences twisting and expansion due to sustained 5-HT binding to both its primary and complimentary faces (see section *3.2, Structural Overview)*. Occupation of the TMD within monomer D (*yellow*) can also be seen in Figure 5C (indicated by a red circle) which depicts lipid density for the three lipid types in 5-$HT_{3A\text{-}5mM}$ over the entire 15 μs and average center of masses for helices M1-M4. Figure 5C demonstrates significantly clustering of SDPC (*cyan*) around the TMD when averaged over the entire 15 μs compared to the two other lipid types. This clustering is not observed initially (after 100 ns) as can be seen in SI Appendix, Figure S14, suggesting the preference of 5-HT_{3A} to a SDPC-rich region of the membrane.

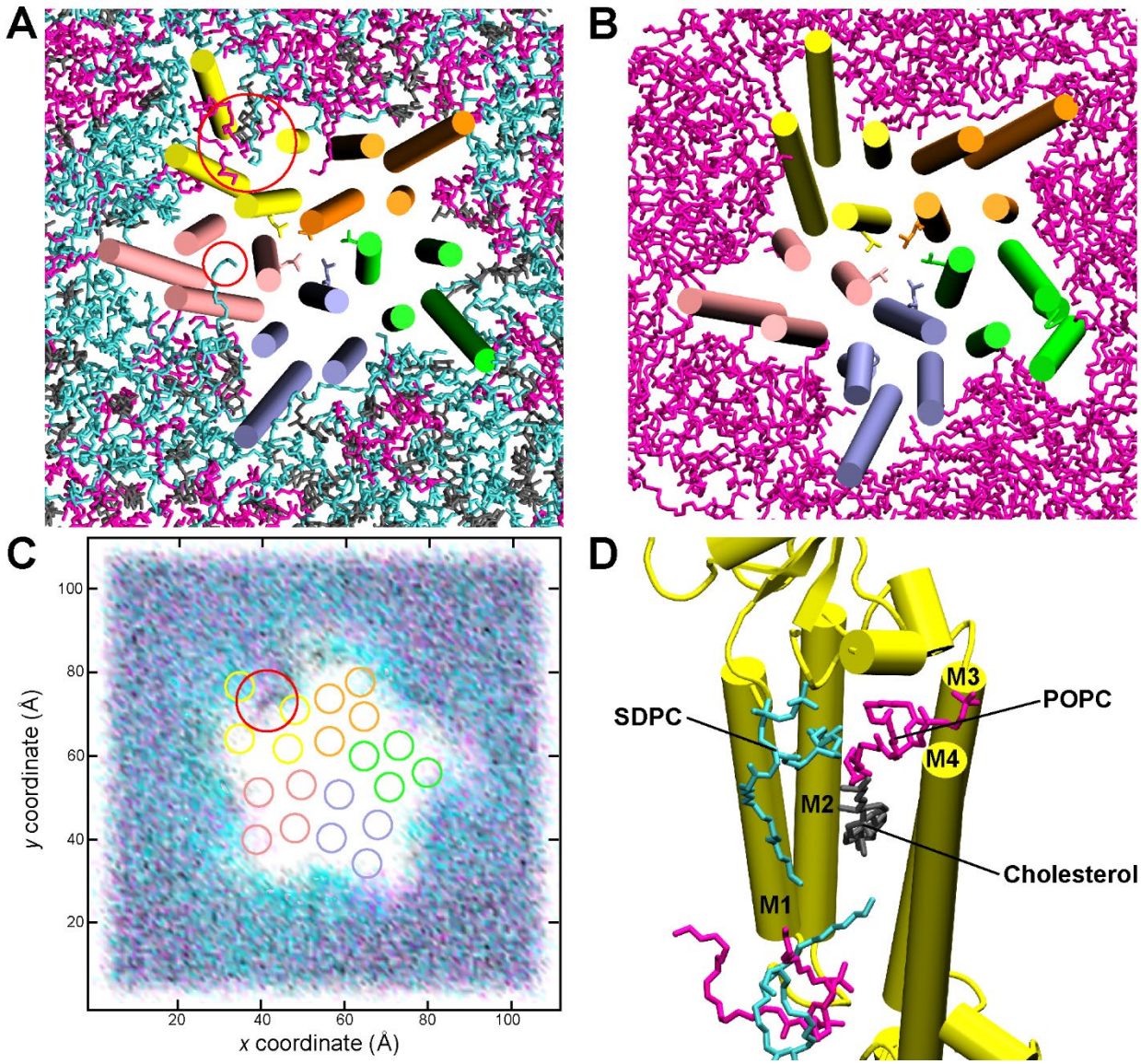

Figure 5. (A) Representative snapshot of 5-HT$_{3A\text{-}5mM}$ colored by monomer (A, *green;* B, *purple*; C, *pink*; D, *yellow*; E, *orange)* depicting transient penetration of the TMD by 1-stearoyl-2-docosahexaenoyl-sn-glyerco-3-phosphocholine (SDPC, *cyan*) and sustained penetration by 1-palmitoyl-2-oleoyl-SN-glycero-3-phosphocholine (POPC, *magenta*), SDPC, and cholesterol (*gray*). (B) Representative snapshot of 5-HT$_{3A\text{-}5mM\text{-}POPC}$ depicting no such penetration when only POPC is present. (C) Lipid density over 15 μs for 5-HT$_{3A\text{-}5mM}$ depicting clustering of SDPC around the TMD and sustained penetration of the TMD. (D) Snapshot of 5-HT$_{3A\text{-}5mM}$ monomer D (*yellow*) shown as secondary structure with penetrating lipids shown as sticks and other lipids removed for clarity.

SI Appendix, Figure S15 demonstrates the relationship between the expansion of the intra-helical space within helices M1-M4 of monomer D, represented by the area formed between a quadrilateral whose four corners are the center of masses of these helices, and lipids that penetrate the intra-helical space as it expands. At the onset of this expansion at around 5 μs, the saturated

tail of a SDPC lipid packs into the intra-helical space, followed by the saturated tail of a POPC lipid that also packs into the intra-helical space at around 6 μs. Over the next six microseconds, the entire POPC lipid packs within the intra-helical space, which is followed by the packing of a second POPC lipid that replaces the saturated tail of the SDPC lipid. This second POPC lipid is subsequently replaced by a single cholesterol at around 12 μs, followed by the packing of a SDPC lipid at around 13 μs into the intra-helical space. Finally, the packing of two additional lipids, one POPC and one SDPC lipid, into the intra-helical space, but towards the bottom of this space to result in the final conformation observed in Figure 5D, which is stable for the remaining 3 μs of the simulation. This packing of three different lipid types stabilizes the final conformation of monomer D and is not observed in any other monomers in this replicate or in the 5-$HT_{3A\text{-}Apo}$ and 5-$HT_{3A\text{-}15mM}$ simulations.

In addition to the monomer D-penetrating cholesterol, which demonstrated sustained hydrogen bonding to Y442 on M4-D, two more cholesterols were identified as hydrogen bonding with a Glu residue on M3-A and an Arg residue on M4-B, respectively, for the final 10 μs of the simulation, though no significant changes in 5-HT_{3A} structure were associated with the binding of these cholesterols to the TMD. Notably, the sustained hydrogen bonding of cholesterol to Y442 of M4-D was only made possible through the trapping of cholesterol via π-π interactions with monomer D (SI Appendix, Figure S16). The first stable interaction with monomer D was π-π stacking with F439 of M4-D for ≈ 50 ns, which transitioned to π-π stacking with F242 of M1 for ≈ 50 ns and finally to hydrogen bonding with Y442 (SI Appendix, Figure S16). Direct hydrogen bonding with Y442 would likely not be possible without first π-π stacking with Y442 and/or F439 which face outwards into the membrane on the M4 and M1 helices, respectively. The end result is a stable binding pocket for cholesterol within monomer D of the TMD, which maintains the final conformation of the monomer (SI Appendix, Figure S17).

4 Discussion

In this work, we performed all-atom MD simulations using the first resolved structure of 5-HT_{3A}, PDB ID: 4PIR (16). This allowed both the observation of an equilibrated membrane-bound conformation of the pLGIC, and the allosteric regulation of its structure by 5-HT. These microsecond-scale simulations permitted the depiction, for the first time, of a dynamic representation of 5-HT binding, and allosteric regulation during the pre-activation or priming of

5-HT_{3A}. We propose that a pre-active rather than fully activated state was observed because the ion channel through 5-HT_{3A} remained closed to ion translocation even with stable binding of two 5-HT ligands in the five possible binding pockets on the ECD. During this state, a twisting and expansion of the 5-HT_{3A} monomer bound on both sides by these 5-HT was observed, indicative of the channel being primed for activation. However, this priming did not result in channel opening across the TMD region of the pore due to a constriction between the 9' and 16' rings. Between the 9' and 16' rings, water did not penetrate differently between the apo vs. 5HT bound conformations (Figure 2A, E and SI Appendix, Figure S18). The observed structural changes during 5-HT binding is in agreement with the proposed mechanism of pLGIC activation (14). However, because only two 5-HT ligands remained bound for the full 15 μs simulation, with the other three 5-HT ligands transiently bound, full activation of the channel was not observed. This is in agreement with kinetic models of experimental data that indicate at least three 5-HT ligands must remain bound to achieve a measurable current through 5-HT_{3A} (9, 34).

Notably, the kinetic models of 5-HT_{3A} that best describe experimental data require the inclusion of a pre-active state, designated by 5-HT binding that primes the pLGIC for activation (9, 34), proposed to enhance cooperativity (39, 40). While we observed the transition of a bound 5-HT neighboring a second bound 5-HT to a less enthalpically favorable orientation, the entropic favorability of this orientation is difficult to obtain with limited sampling. Therefore, we cannot fully quantify whether 5-HT binding caused higher affinity for 5-HT in a neighboring binding pocket as hypothesized for other pLGICs (39, 40). We do, however, report other conformational changes from 5-HT binding which appear to prime the ECD-TMD interface for channel activation, such as the stabilization of an open conformation of the M2 helix through stabilization of the M2-M3 loop of the TMD by the β1-β2 and β8-β9 loops of the ECD, in agreement with previous observation (18, 20). The stable binding of only two of five 5-HT ligands to 5-HT_{3A} further allowed us to report for the first time differences in allosteric regulation based on monomers that are bound on either the primary, complimentary, or both faces by 5-HT.

Critically, our observation of 5-HT_{3A} pre-activation is based on the assumption that the starting structure, PDB ID: 4PIR (16), represents a resting state and not a desensitized state as previously hypothesized (17). To this end, we ensured the accurate representation of 5-HT_{3A} *in silico* by embedding the pLGIC in a lipid membrane representative of the native membrane, measuring structural equilibration with RMSD, and comparing differences between 5-HT-bound and *apo*

conformations. The lipid membrane environment, including the adequate packing of lipids in the membrane, has been shown to be essential for accurate MD simulations of ion channels, and can even regulate ion channel conductance (41-46). Here, we report for the first time the use of a well-equilibrated POPC/SDPC/Cholesterol lipid membrane that mimics the native neuronal membrane (specific benefits of adding SDPC and cholesterol are presented at the end of the discussion). We found that 250 ns of equilibration was necessary to achieve membrane equilibration, i.e. lipid packing, as reported through SA/lipid (SI Appendix, Figure S2) for the POPC/SDPC/Cholesterol membranes (as well as pure POPC membranes). This equilibration is important because if the membrane is not natively packed it promotes the TMD to spontaneously expand outwards into the membrane, which may be erroneously observed as channel opening. Previous simulations of 5-HT_{3A} that used pure POPC membranes (18-20) have not reported metrics such as SA/lipid that would indicate sufficient lipid packing, and may have erroneous conclusions based on less packed membranes.

Protein structure determined through crystallization is not necessarily representative of the native structure under physiological conditions, especially when nanobodies are needed to resolve the structure, such as the 5-HT_{3A} structure used in this work (16). To reconcile this, we report structural changes from a crystalized structure of 5-HT_{3A} to a more native state, which we report as requiring up to 12 μs to relax. Notably, *apo* 5-HT_{3A} took the most time to stabilize (12 μs), whereas 5-HT-bound forms took less time (8 μs – 10 μs), which we suggest is due to loop *c* and other binding pocket residues that are restrained by 5-HT binding, but exhibit greater flexibility without 5-HT in the *apo* case. This essential RMSD metric to confirm 5-HT_{3A} equilibration in the lipid membrane was not reported for previous simulations that only equilibrated 5-HT_{3A} for at most 60 ns, whereas our results indicate that these timescales are orders of magnitude less than what is required to achieve structural equilibration (18-20). Similarly to under-equilibrated lipid membranes, incomplete equilibration of protein structure can lead to the erroneous observations regarding 5-HT_{3A} structure.

A conductive or open state can be easily discerned from the translocation of hydrated ions across the pLGIC. However, assigning a channel state to a closed pLGIC (i.e. a pre-active, desensitized, or resting state) is more difficult, requiring a comparison between the *apo* and ligand-bound conformations. The pore radius profiles for all four systems reported in this work demonstrate that the TMD pore closes for both *apo* and 5-HT-bound conformations of 5-HT_{3A} to

less than the radius of a hydrated K^+ ion, resulting in a closed conformation. In 5-HT3A-Apo, this closure is symmetric through the TMD, and there is little change to the pore radius profile of the ECD compared to the crystalized conformation, suggesting a resting state either before activation or after desensitization (Figure 2). Similarly, previous MD simulations of *apo* 5-HT_{3A} (PDB IDs: 4PIR and 6BE1) also report that the *apo* conformation remains closed to ion translocation and resembles a resting state (18, 20).

Conversely to 5-$HT_{3A\text{-}Apo}$, 5-$HT_{3A\text{-}5mM}$ demonstrated asymmetric closure through the TMD in combination with evidence of pre-activation, which has not been observed previously for 5-HT_{3A} (18-20). Notably, asymmetric closure in 5-$HT_{3A\text{-}5mM}$ was observed with the expansion of at least one monomer through the TMD due to 5-HT-binding. Therefore, we do not believe the conformation represents a desensitized state which would not demonstrate an allosteric response from 5-HT binding, in contrast to a previous hypothesis (17). Previous MD simulations of 5-HT_{3A} have not conclusively demonstrated activation of the pLGIC with five 5-HT ligands bound for the entire simulation, including a lack of maintaining an initially open conformation in an activated state (18-20). Evidence of partial activation that was observed may be an artifact of insufficient protein equilibration, insufficient lipid packing, and the application of artificial restraints that bias the structure of 5-HT_{3A} in a given conformation (18-20).

In short, closure through the TMD of 5-HT_{3A} is not unprecedented, but the timescales used in this work, an order of magnitude greater than any previous work, allowed us to observe the unbinding and rebinding of 5-HT to 5-HT_{3A}, and the priming of 5-HT_{3A} after the structure was allowed to equilibrate to a more native conformation. Nevertheless, it is possible that the timescales used in this work are still insufficient to definitively observe 5-HT_{3A} pre-activation; therefore, we can only conclude that 5-HT mediated pre-activation is suggested by these simulations. The fastest activation time for 5-HT_{3A} is on the scale 1 – 10 ms (9, 34), which is at least two orders of magnitude greater than the time-scales used in this work.

While the unbinding of 5-HT from 5-HT_{3A} is a novel observation, we do note that ligand unbinding has been observed previously for other pLGICs including GluCl (14), where four of five glutamate ligands became unbound before 500 ns, with only one rebinding transiently over the final 1 μs. This unbinding resulted in channel closure similarly to that observed in this work, described as ‘spontaneous relaxation of the channel’, and supported a conclusion that crystalized conformations of pLGICs may be in a pre-active state that require microsecond timescales to

observe priming or pre-activation (14). While this work stands as a demonstration of the ability of microsecond time-scale simulations to capture conformational changes of ligand-gated ion channels, such as pre-activation of 5-HT_{3A}, subsequent work should aim to reproducibly demonstrate this mechanism or other mechanisms such as desensitization or inhibition over multi-microsecond timescales.

Lastly, evidence demonstrating the direct effects of lipids on 5-HT_{3A}, including from cholesterol and PUFA lipids, is lacking compared to other pLGICs (25). We report sustained interactions between cholesterol and the TMD of 5-HT_{3A}, specifically that cholesterol, along with POPC and SPDC, penetrate the TMD of 5-$HT_{3A\text{-}5mM}$ monomer D (SI Appendix, Figure S15) as it twists and expands due to 5-HT binding and stabilize it in a presumed pre-active state (SI Appendix, Figure S17). This suggests that lipid types other than POPC are required to modulate the 5-$HT_{3A\text{-}5mM}$ response to 5-HT binding including the stabilization of the pre-active state. We also observed hydrogen bonding between cholesterol and M4, which also has not been previously reported, and appears critical to catch cholesterol through π-π bonding before it is able to fully penetrate the TMD. Experimentally, cholesterol has been included in lipid membranes to study the structure of 5-HT_{3A} (16, 47), but few conclusions have been reported besides the distribution of 5-HT_{3A} in the membrane changing from evenly distributed to tightly packed clusters as a result of the removal of cholesterol (47). However, because the structure of 5-HT_{3A} is largely homologous to other pLGICs including the nAChR, GLIC, and GABA receptors, whose amplitude of channel conductance and rate of desensitization are regulated by cholesterol and PUFA lipids (25-29), (35-38), it is likely that cholesterol and PUFA lipids play a role in regulating the structure and function of 5-HT_{3A}. Notably, MD simulations have previously demonstrated a binding site for cholesterol on GABA (35), which demonstrated that cholesterol interacts with the M2 helix of the TMD, strongly suggesting the regulation of channel conductance. While we did not observe any direct interactions between M2 and cholesterol, we note that in (35) cholesterol was docked at the M2 helix, as opposed to our simulations which required the diffusion of lipids to penetrate 5-HT_{3A5mM} monomer D. Additional simulations of 5-HT_{3A} will be needed to fully understand the role of cholesterol and PUFA lipids in regulating 5-HT_{3A} function, including ones that leverage the potential cholesterol binding site by homology to GABA (35).

Cholesterol interactions were also compared to a recent crystal structure of nAChR (PDB ID: 6CNJ (54)). The cholesterol interactions between nAChR and 5-HT_{3A} appear very similar. In both

cases, cholesterol interacts with the protein between the M1 and M4 helices (though also between the M2 and M3 helices in the case of nAChR) and is oriented vertically in the same orientation, i.e. with the hydroxyl group pointing downwards. However, because the cholesterol interactions examined in this work were of the pre-activated state instead of the "agonist-bound desensitized state" as in the case of nAChR (54), the cholesterol in this work appears to penetrate a pre-activated conformation of a monomer by binding between the M1 and M4 helices, whereas in the case of nAChR it appears to stabilize a desensitized conformation of a monomer by binding the periphery of the M1 and M4 helices.

Methods

The CHARMM-GUI *Membrane Builder* (48) was used to build protein-membrane systems (Figure 1A) with 5-HT_{3A} (PDB ID: 4PIR (16)) and lipid membranes composed of either 7:7:6 SDPC/POPC/cholesterol, which has been shown to mimic the neural membrane environment (24), or POPC. The unresolved M2-M3 loop was added using *Modeller (49)*. The 57 unresolved intracellular and intrinsically disordered residues linking the M4 helix to the MX helix were not added; however, the membrane served as a scaffold and ensured that the M4 helix did not separate from the rest of the TMD. Stochastic movement of the M4 helices was quantified through the distances between the center of masses M4 and M1, and the M4 and M3 helices (SI Appendix, Figure S19). SI Appendix, Figure S19 demonstrates that such movement is similar for the M3-M4 and M1-M4 distances in 5-$HT_{3A\text{-}Apo}$ and 5-$HT_{3A\text{-}5mM}$, where these distances are maintained in the all cases, except for the M3-M4 distance in monomer E of the *apo* case, which after shifting at around 13 μs, achieves a new equilibrium distance for the rest of the simulation. These figures demonstrate the minimal wandering of M4 helices, and their overall equilibration.

These simulations used the TIP3P water model (50, 51) with the CHARMM36 (C36) FF for lipids (21, 22) and for proteins (23). The CHARMM general FF (CGenFF) was used to obtain initial parameters for 5-HT (52), which were modified based on free energy perturbation (FEP). FEP was used to determine ΔG° for 5-HT in aqueous and octanol phases which were used as inputs for the relationship $log\ P_{Oct/Wat} = \frac{(\Delta G°_{Wat} - \Delta G°_{Oct})}{RT}$, where log $P_{Oct/Wat}$ is the base-ten logarithm for the partition coefficient, a ratio of the concentrations of 5-HT between water and octanol, $\Delta G°_{Wat}$ and $\Delta G°_{Oct}$ are the Gibbs free energies of 5-HT in water and octanol in kcal mol^{-1}, respectively, R

is the gas constant in kcal K^{-1} mol^{-1}, and T is temperature in K. The partition coefficient $P_{o/w}$ is experimentally determined for 5-HT, therefore $\Delta G°_{Wat}$ and $\Delta G°_{Oct}$ calculated from FEP must yield the experimentally determined $P_{Oct/Wat}$ using the above relationship. To achieve this end, the charge parameters of 5-HT are changed from those initially provided by CGenFF to satisfy these conditions. Next, 5-HT was docked to 5-HT_{3A} using *AutodockVina* and including flexible side chains (53). Please see SI Appendix for more details.

Author Contributions

N.B.G. designed and performed research, analyzed data, and prepared the manuscript. A.B. aided in designing research, analyzing data, and preparing the manuscript. J.B.K. aided in designing research, analyzing data, and preparing the manuscript.

Data availability statement

All data discussed in the paper will be made available to readers upon request to corresponding author.

Acknowledgments

This research is supported by the National Institute of Standards and Technology (NIST) grant 70NAHB15H023. Several high performance resources were used in this research: 1. Deeptought2 which is maintained by the Division of Information Technology at the University of Maryland, 2. Stampede via our Extreme Science and Engineering Discovery Environment (XSEDE) allocation by grant number MCB-100139 and Raritan at NIST. 3. The Anton 2 supercomputer, on loan to Carnegie Mellon University (CMU) from D. E. Shaw Research, LLC for use as outlined in grant number R01GM116961 from the National Institutes of Health to CMU through the Biomedical Applications Group at the Pittsburgh Supercomputing Center, by grant number PSCA18011P.

References

1. Yakel J (2000) The 5-HT 3 Receptor Channel: Function, Activation and Regulation. *Pharmacology of ionic channel function: activators and inhibitors*, (Springer), pp 541-560.
2. Thompson AJ & R Lummis S (2006) 5-HT3 receptors. *Current pharmaceutical design* 12(28):3615-3630.
3. Yakel JL & Jackson MB (1988) 5-HT3 receptors mediate rapid responses in cultured hippocampus and a clonal cell line. *Neuron* 1(7):615-621.
4. Gross C & Hen R (2004) Genetic and environmental factors interact to influence anxiety. *Neurotoxicity research* 6(6):493-501.

5. Anguelova M, Benkelfat C, & Turecki G (2003) A systematic review of association studies investigating genes coding for serotonin receptors and the serotonin transporter: II. Suicidal behavior. *Molecular psychiatry* 8(7):646.
6. Thompson AJ & Lummis SC (2007) The 5-HT3 receptor as a therapeutic target. *Expert opinion on therapeutic targets* 11(4):527-540.
7. Walstab J, Rappold G, & Niesler B (2010) 5-HT 3 receptors: role in disease and target of drugs. *Pharmacology & therapeutics* 128(1):146-169.
8. Gielen M & Corringer PJ (2018) The dual-gate model for pentameric ligand-gated ion channels activation and desensitization. *The Journal of physiology* 596(10):1873-1902.
9. Corradi J, Gumilar F, & Bouzat C (2009) Single-channel kinetic analysis for activation and desensitization of homomeric 5-HT3A receptors. *Biophysical journal* 97(5):1335-1345.
10. Nemecz A, Prevost MS, Menny A, & Corringer P-J (2016) Emerging molecular mechanisms of signal transduction in pentameric ligand-gated ion channels. *Neuron* 90(3):452-470.
11. Nury H*, et al.* (2010) One-microsecond molecular dynamics simulation of channel gating in a nicotinic receptor homologue. *Proceedings of the National Academy of Sciences*.
12. Calimet N*, et al.* (2013) A gating mechanism of pentameric ligand-gated ion channels. *Proceedings of the National Academy of Sciences*:201313785.
13. Chiodo L, Malliavin T, Maragliano L, & Cottone G (2017) A possible desensitized state conformation of the human α7 nicotinic receptor: A molecular dynamics study. *Biophysical chemistry* 229:99-109.
14. Martin NE, Malik S, Calimet N, Changeux J-P, & Cecchini M (2017) Un-gating and allosteric modulation of a pentameric ligand-gated ion channel captured by molecular dynamics. *PLOS Computational Biology* 13(10):e1005784.
15. Cerdan AH, Martin NÉ, & Cecchini M (2018) An Ion-Permeable State of the Glycine Receptor Captured by Molecular Dynamics. *Structure* 26(11):1555-1562. e1554.
16. Hassaine G*, et al.* (2014) X-ray structure of the mouse serotonin 5-HT3 receptor. *Nature* 512(7514):276-281.
17. Basak S*, et al.* (2018) Cryo-EM structure of 5-HT 3A receptor in its resting conformation. *Nature communications* 9(1):514.
18. Basak S, Gicheru Y, Rao S, Sansom MS, & Chakrapani S (2018) Cryo-EM reveals two distinct serotonin-bound conformations of full-length 5-HT 3A receptor. *Nature*:1.
19. Yuan S, Filipek S, & Vogel H (2016) A Gating Mechanism of the Serotonin 5-HT 3 Receptor. *Structure* 24(5):816-825.
20. Polovinkin L*, et al.* (2018) Conformational transitions of the serotonin 5-HT 3 receptor. *Nature*:1.
21. Klauda JB*, et al.* (2010) Update of the CHARMM all-atom additive force field for lipids: Validation on six lipid types. *J. Phys. Chem. B* 114:7830-7843.
22. Klauda JB, Monje V, Kim T, & Im W (2012) Improving the CHARMM Force Field for Polyunsaturated Fatty Acid Chains. *J. Chem. Phys. B* 116:9424-9431.
23. Best RB*, et al.* (2012) Optimization of the additive CHARMM all-atom protein force field targeting improved sampling of the backbone ϕ, ψ and side-chain χ1 and χ2 dihedral angles. *Journal of chemical theory and computation* 8(9):3257-3273.
24. Shan J, Khelashvili G, Mondal S, Mehler EL, & Weinstein H (2012) Ligand-dependent conformations and dynamics of the serotonin 5-HT2A receptor determine its activation and membrane-driven oligomerization properties. *PLoS computational biology* 8(4):e1002473.

25. Fantini J & Barrantes FJ (2009) Sphingolipid/cholesterol regulation of neurotransmitter receptor conformation and function. *Biochimica et Biophysica Acta (BBA)-Biomembranes* 1788(11):2345-2361.
26. Cecchini M & Changeux J-P (2015) The nicotinic acetylcholine receptor and its prokaryotic homologues: Structure, conformational transitions & allosteric modulation. *Neuropharmacology* 96:137-149.
27. Brannigan G, Hénin J, Law R, Eckenhoff R, & Klein ML (2008) Embedded cholesterol in the nicotinic acetylcholine receptor. *Proceedings of the National Academy of Sciences* 105(38):14418-14423.
28. Barrantes FJ (2007) Cholesterol effects on nicotinic acetylcholine receptor. *Journal of neurochemistry* 103:72-80.
29. Baenziger JE, Domville JA, & Therien JD (2017) The role of cholesterol in the activation of nicotinic acetylcholine receptors. *Current topics in membranes*, (Elsevier), Vol 80, pp 95-137.
30. Vanommeslaeghe KH, E. Acharya, C. Kundu, S. Zhong, S. Shim, J. E. Darian, E. Guvench, O. Lopes, P. Vorobyov, I. and MacKerell, Jr. A.D. (2010) CHARMM General Force Field (CGenFF): A force field for drug-like molecules compatible with the CHARMM all-atom additive biological force fields. *Journal of Computational Chemistry* 31:671-690.
31. Kucerka N, Nieh MP, & Katsaras J (2011) Fluid phase lipid areas and bilayer thicknesses of commonly used phosphatidylcholines as a function of temperature. *Biochim. Biophys. Acta Biomembrane* 1808(11):2761-2771.
32. Alwarawrah M, Dai J, & Huang J (2010) A molecular view of the cholesterol condensing effect in DOPC lipid bilayers. *The journal of physical chemistry B* 114(22):7516-7523.
33. Melis C, Bussi G, Lummis SC, & Molteni C (2009) Trans− cis Switching Mechanisms in Proline Analogues and Their Relevance for the Gating of the 5-HT3 Receptor. *The Journal of Physical Chemistry B* 113(35):12148-12153.
34. Corradi J & Bouzat C (2014) Unraveling mechanisms underlying partial agonism in 5-HT3A receptors. *Journal of Neuroscience* 34(50):16865-16876.
35. Hénin J, Salari R, Murlidaran S, & Brannigan G (2014) A predicted binding site for cholesterol on the GABAA receptor. *Biophysical journal* 106(9):1938-1949.
36. Yoluk Ö, Brömstrup T, Bertaccini EJ, Trudell JR, & Lindahl E (2013) Stabilization of the GluCl ligand-gated ion channel in the presence and absence of ivermectin. *Biophysical journal* 105(3):640-647.
37. Gicheru YW, Basak S, & Chakrapani S (2017) Structural Mechanisms Underlying PUFA Modulation in Pentameric Ligand Gated Ion Channels. *Biophysical Journal* 112(3):320a.
38. Basak S, Schmandt N, Gicheru Y, & Chakrapani S (2017) Crystal structure and dynamics of a lipid-induced potential desensitized-state of a pentameric ligand-gated channel. *Elife* 6:e23886.
39. Burzomato V, Beato M, Groot-Kormelink PJ, Colquhoun D, & Sivilotti LG (2004) Single-channel behavior of heteromeric α1β glycine receptors: an attempt to detect a conformational change before the channel opens. *Journal of Neuroscience* 24(48):10924-10940.
40. Lape R, Colquhoun D, & Sivilotti LG (2008) On the nature of partial agonism in the nicotinic receptor superfamily. *Nature* 454(7205):722.

41. Aguilella VM, Carmina Verdiá-Báguena, and Antonio Alcaraz (2014) Lipid charge regulation of non-specific biological ion channels. *Physical Chemistry Chemical Physics* 16(9):3881-3893.
42. Guros NB, Balijepalli AK, & Klauda JB (2018) The Role of Lipid Interactions in Accurate Simulations of the alpha-hemolysin Transporter.
43. Tucker SJ & Baukrowitz T (2008) How highly charged anionic lipids bind and regulate ion channels. *The Journal of general physiology* 131(5):431-438.
44. Valenzuela SM*, et al.* (2013) Regulation of the membrane insertion and conductance activity of the metamorphic chloride intracellular channel protein CLIC1 by cholesterol. *PLoS One* 8(2):e56948.
45. Noriko Tomitaa MMM, David J. Niedzwieckia, Makoto Ohtab, Liviu Movileanu (2013) Does the lipid environment impact the open-state conductance of an engineeredβ-barrel protein nanopore? *Biochimica et Biophysica Acta* 1828(3):1057-1065.
46. Corradi V*, et al.* (2018) Emerging Diversity in Lipid–Protein Interactions. *Chemical reviews*.
47. Kudryashev M*, et al.* (2016) The structure of the mouse serotonin 5-HT3 receptor in lipid vesicles. *Structure* 24(1):165-170.
48. S. Jo TK, V. G. Iyer, W. Im (2008) CHARMM-GUI: A web-based graphical user interface for CHARMM. *Journal of Computational Chemistry* 29(11):1859-1865.
49. B. Webb AS (2014) Comparative Protein Structure Modeling Using Modeller. *Current Protocols in Bioinformatics*:5.6.1-5.6.32.
50. Durell SR, Brooks BR, & Bennaim A (1994) Solvent-Induced Forces between Two Hydrophilic Groups. *J. Phys. Chem.* 98:2198-2202.
51. Jorgensen WL, Chandrasekhar J, Madura JD, Impey RW, & Klein ML (1983) Comparison of Simple Potential Functions for Simulating Liquid Water *J. Chem. Phys.* 79:926-935.
52. Trott O & Olson AJ (2010) AutoDock Vina: improving the speed and accuracy of docking with a new scoring function, efficient optimization, and multithreading. *Journal of computational chemistry* 31(2):455-461.
53. Vanommeslaeghe K*, et al.* (2010) CHARMM general force field: A force field for drug-like molecules compatible with the CHARMM all-atom additive biological force fields. *Journal of computational chemistry* 31(4):671-690.
54. Walsh, R. M., Roh, S. H., Gharpure, A., Morales-Perez, C. L., Teng, J., & Hibbs, R. E. (2018). Structural principles of distinct assemblies of the human α4β2 nicotinic receptor. *Nature*, *557*(7704), 261.